Arbitrary-oriented tunnel lining defects detection from GPR images using deep CNN

Jing Wang[a], Jiaqi Zhang[a], Anthony G. Cohn[b], Zhengfang Wang[a,*], Hanchi Liu[a], Wenqiang Kang[a], Peng Jiang[c], Fengkai Zhang[d], Kefu Chen[a], Wei Guo[a], Yanfei Yu[a]

[a] *School of Control Science and Engineering, Shandong University, Jinan, 250061, China*
[b] *School of Computing, University of Leeds, Leeds, LS29JT, UK*
[c] *School of Qilu Transportation, Shandong University, Jinan, 250061, China*
[d] *Geotechnical and Structural Engineering Research Center, Shandong University, Jinan, 250061, China*

[*] Corresponding author
Email addresses: wangjingkz@sdu.edu.cn (Jing Wang), 201934530@mail.sdu.edu.cn (Jiaqi Zhang), A.G.Cohn@leeds.ac.uk (Anthony G. Cohn), wangzhengfangsdu@hotmail.com (Zhengfang Wang), 201934495@mail.sdu.edu.cn (Hanchi Liu), 201934483@mail.sdu.edu.cn (Wenqiang Kang), sdujump@gmail.com (Peng Jiang), sduzfk@163.com (Fengkai Zhang), ckf_neuq@163.com (Kefu Chen), 1773725538@qq.com (Wei Guo), 201934527@mail.sdu.edu.cn (Yanfei Yu)

A B S T R A C T

Tunnel lining internal defect detection is essential for the safe operation of tunnels. This paper presents an automatic scheme based on rotational region deformable convolutional neural network (R^2DCNN) and Ground Penetrating Radar (GPR) images for the accurate detection of defects and rebars with arbitrary orientations. The R^2DCNN comprises inter-related modules, specifically, deformable convolution, feature fusion, and rotated region detection modules. In this study, synthetic GPR images, including rebars and various structural defects with different permittivities, as well as real GPR images obtained by model experiments, were constructed for the R^2DCNN. Improved results were obtained while testing the R^2DCNN on GPR images in comparative experiments. The mean average precision of the R^2DCNN was enhanced by 8.21% compared to the R^2CNN on synthetic GPR images. The R^2DCNN showed satisfactory results in on-site experiments, which demonstrated the applicability of the R^2DCNN to practical tunnels.

A R T I C L E I N F O

Keywords: Ground Penetrating Radar; Arbitrary-oriented defect detection; Automation; Deep learning; Tunnel inspection

1. Introduction

Tunnels progressively deteriorate due to ageing, environmental factors, man-made and natural influences, inadequate or poor maintenance, and deferred repairs [1-2]. Consequently, structural defects, including cracks, voids, and separations, occur in the tunnel lining, which can even cause partial collapses in tunnels and significantly affects the long-term and safe operation of tunnels. For instance, the collapse of the Sasago Tunnel in Tokyo killed nine people in 2012 [3]. Therefore, routine inspections and evaluations of tunnels are essential to ensure their safe operation.

Ground Penetrating Radar (GPR), a non-destructive detection tool that can obtain subsurface images, has high efficiency, high anti-interference level, and strong penetrating ability; it has been widely used in detecting subsurface abnormal objects [4]. The electromagnetic waves transmitted by GPR are reflected to form the B-Scan profile after hitting media with different electromagnetic properties. Therefore, the detection of subsurface abnormal objects can be considered as the detection of abnormal GPR signals, such as the reflected signals from subsurface abnormal objects of the B-Scan. In tunnel lining detection, the diagnostic interpretation of GPR images carried out by an experienced analyst is time-consuming and error-prone, which tends to result in poor quality inspections. An automated, cost-effective, and exhaustive inspection of tunnels would improve short and long-term security, and increase productivity [1, 5]. Therefore, automated inspection would become an important means of infrastructure inspection and would gradually become the trend for development in the future. Furthermore, automatic detection methods are a key part of automated inspection. It is necessary to explore a faster, efficient, practical, and automatic detection method to improve automated infrastructure inspections.

In the past few years, certain signal and image processing technologies, such as edge detection, Hough transform, and migration technologies, have been utilized for the automatic detection of abnormal GPR signals [6-9]. Thereafter, machine learning techniques, such as neural networks, support vector machines, grouping techniques, and genetic algorithms, have been utilized to detect subsurface abnormal objects using GPR images [10-13], resulting in effective detection performance. However, the afore-mentioned methods have been commonly observed to lack the ability to recognize multiple waves induced by water-bearing defects in complex GPR images and rely on parameter settings and handcrafted features. Deep learning has been effectively applied to recognize abnormal objects in GPR images and has attracted considerable research interest in various scientific disciplines. For road inspection, Xu et al. [14] integrated a feature cascade, an adversarial spatial dropout network, and the Soft-NMS algorithm into Faster R-CNN to improve the effectiveness of railway subgrade defect detection. Tong et al. [15] utilized the deep learning model of network in networks and GPR data to identify pavement distress types and measure the distress locations and sizes, which produced reasonable stability with different transmitting frequencies, numbers of samples per trace, and pavement structures. For rebar inspection, Xiang et al. [16] automatically detected the rebars of concrete structures using AlexNet and GPR images. The authors also evaluated the effects of different rebar arrangements and window sizes on the results. Similarly, Dinh et al. [17] combined conventional image processing techniques and a deep Convolutional Neural Network (CNN) for rebar recognition. These image processing techniques were used to localize pixels containing potential rebar peaks, and the CNN was employed to classify window images that were extracted from GPR images surrounding the potential pixels. For pipeline inspection, Alvarez et al. [18] used a deep learning framework to convert GPR images into subsurface permittivity maps to realize the intuitive display of subsurface images of sewer crowns. Furthermore, Ko et al. [19] used Faster R-CNN to detect buried pipelines in GPR images and adopted a data augmentation strategy for GPR images.

The recognition of GPR images has been successfully accomplished using deep learning, and it has been widely applied in various fields. To detect abnormal objects within a tunnel lining, Yang et al. [20] employed GPR data and a CNN to conduct defect segmentation for tunnel lining internal defects, thereby achieving visual display of the tunnel lining internal structure. Their method requests pixel-level labels to perform data annotation. However, owing to the uncertainty of the tunnel lining internal structure in practical situations, it is difficult to obtain a corresponding structural model from real GPR data collected from tunnels, thereby making it challenging to use pixel-level labels. Thus, the application of this method to practical situations is limited owing to the difference between synthetic and real GPR data. CNNs used for object detection can identify events or implications of GPR images that are difficult to annotate using pixel-level labels. For example, Xu et al. [21] constructed a convolutional neural network (GA-RCNN) which integrated the mechanism of guiding anchoring based on the two-stage object detection algorithm to accurately recognize the locations of the voids using GPR images in tunnels. However, certain challenges related to the internal abnormal object detection of tunnel linings still exist, such as:

(1) Unlike object detection in natural images, wherein the objects have clear boundaries, abnormal objects in GPR images commonly exhibit complex reflected signals with diffraction signatures. Even worse, complex irregular tunnel lining defects, particularly crack defects, may have arbitrary distributions (Fig. 1). Therefore, it is crucial to accurately delineate the locations of defects with arbitrary orientations from GPR images with relatively blurred boundaries.

(2) Owing to the diversity of tunnel lining defects, as well as multiple waves and scattering induced by water-bearing defects, the recorded GPR images can be rather complicated, with various reflected signals from tunnel lining defects. Defects in the same category may produce quite different GPR images, as shown in Fig. 1. Thus, it is essential for deep learning networks to have powerful feature representation and feature fusion abilities to extract rich features from various GPR images.

(3) Owing to unpredictable interference in the real world, real GPR images are inevitably accompanied by considerable noise and are more complicated than synthetic GPR images, as shown in Fig. 1. Furthermore, the availability of real GPR images for training deep learning networks is rather limited. Therefore, it is preferable for deep learning networks to learn the geometric transformations of reflected signals from tunnel lining defects adaptively and generalize the trained models for application to real GPR images.

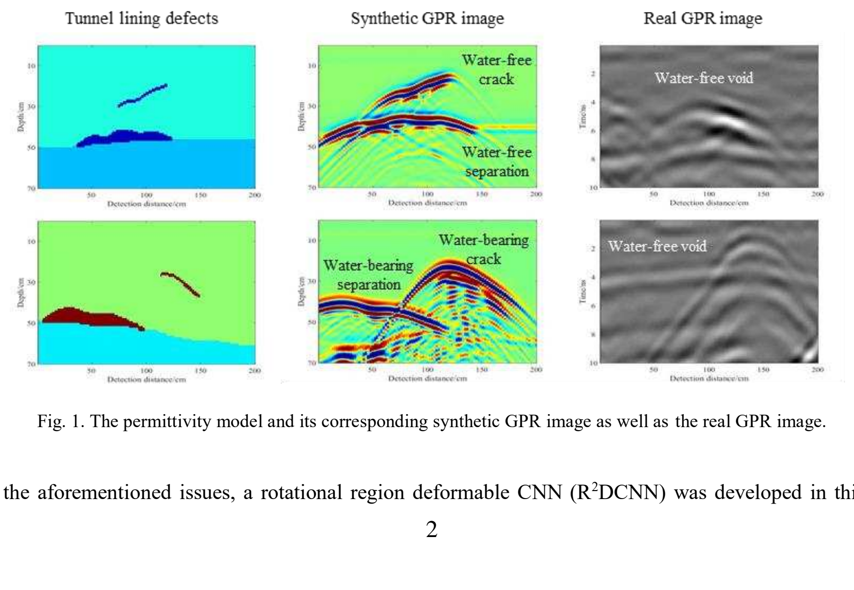

Fig. 1. The permittivity model and its corresponding synthetic GPR image as well as the real GPR image.

To solve the aforementioned issues, a rotational region deformable CNN (R^2DCNN) was developed in this study for the accurate detection of defects and rebars with arbitrary orientations from complex GPR images of tunnel linings. The R^2DCNN comprises inter-related modules, specifically, deformable convolution (DC) [22-23], feature fusion [24-25], and rotated region detection modules [26]. DC enhances the ability to detect abnormal objects with geometric deformations, such as various reflected signals from tunnel lining defects of different sizes and shapes, and enables the adaptive learning ability for diverse real GPR images. Feature fusion for fine-grained feature extraction provides accurate location and shape information for abnormal objects to improve the final detection accuracy of GPR images with blurred boundaries between the object and background. Rotated region detection enables the accurate detection of abnormal objects with arbitrary orientations in GPR images. In this study, synthetic GPR images, including rebars and various structural defects with different permittivities, as well as real GPR images obtained by model experiments, were constructed for the R^2DCNN. A comprehensive comparative experiment was performed to confirm the effectiveness of the R^2DCNN, and a model experiment was subsequently performed to demonstrate the necessity of the R^2DCNN on real GPR images. Furthermore, on-site experiments were employed to describe the implementation process of the R^2DCNN in detail. The defect detection method was verified in engineering and was applicable in practical tunnels, laying a solid foundation for automated inspection of tunnels in the future.

The remainder of this paper is organized as follows: Section 2 describes the dataset, Section 3 introduces the R^2DCNN automatic detection method, Section 4 presents and provides an analysis of the experimental results, Section 5 conducts on-site experiments and applications of the method, and lastly, Section 6 summarizes the contributions and draws certain conclusions.

2. Dataset construction

Considering that GPR images with reflected signals collected from practical tunnels are quite limited, which is not enough for the training of the R2DCNN to realize the accurate detection of tunnel lining defects with arbitrary orientations, lots of GPR images are constructed to improve the adaptability of the proposed method in engineering. This section describes the datasets consisting of synthetic and real GPR images that are built to train, validate, and test the object detection network. Furthermore, it elaborates the process of the GPR image annotation.

2.1. Synthetic GPR data

Tunnel linings containing rebars as well as various structural defects, including voids, cracks, and separations, were modelled. These defects were further divided into water-bearing and water-free defects according to their permittivities and were referred to as tunnel lining abnormal objects in the following sections.

Various objects with irregular borders of different shapes, categories, and permittivities were deployed at various positions. In this study, the permittivities of water-free defects, water-bearing defects, and rebars were 1, 81, and 300, respectively. The permittivities of the lining and surrounding rock were random, i.e., 6–7 and 8–10, respectively [27]. In addition, the interface between the lining and surrounding rock was considered as a rough and irregular surface. The two-dimensional basic permittivity models of the tunnel lining internal structure were established based on the above principles, as illustrated in Fig. 2, which showed that there are various distributions of objects in the permittivity model, including single defects, different combinations of multiple defects and rebars, and water-bearing and water-free defects distinguished by different permittivities as represented by different colors. GPR equipment with dominant frequencies of 400 MHz or 600 MHz was relatively common in tunnel lining detection. Therefore, to increase the diversity of the data and enhance the adaptability of the network, two Ricker wavelets with dominant frequencies of 400 MHz and 600 MHz were used to forward modelling permittivity models based on the finite-difference time-domain method. Finally, synthetic GPR data with 800 sampling steps and 99 traces was obtained. In this work, a total of 1974 synthetic GPR data with different frequencies and conductivities were generated, and it took approximately three days to generate these datasets. Among them, only the conductivity of 59 synthetic GPR data (0.5) with water-bearing defects is different from other data (0.0005) to verify the generalization of the network. The specific defect categories and numbers of the rest of the 1915 synthetic GPR data, including 900 GPR data with a dominant frequency of 600 MHz and 1015 GPR data with a dominant frequency of 400 MHz, are presented in Table 1. The dimensions of the model were 90×220 with a mesh size of 0.01 m. Owing to the absorption boundary conditions of the convolutional perfectly matched layer, the actual model was reduced by 10 meshes on each side. Therefore, the depth and distance of the tunnel lining covered in the synthetic GPR data were 0.7 m and 2 m, respectively. It was difficult to annotate the synthetic GPR data containing direct waves covering some portions of the target areas. Therefore, the direct waves were removed by subtracting the baseline GPR data generated by the model without any abnormal objects. Fig. 2 depicts the permittivity models and their corresponding synthetic GPR data before and after removing the direct waves. Moreover, owing to the diffraction signals appearing on the edges of the reflected signals and the multiple waves and scattering induced by water-bearing defects, GPR images have characteristics that differ from those of natural images. Hence, GPR images were chosen (instead of ImageNet) to pre-train the feature extraction network for classification, thereby making it more adaptive to GPR images. Additional 28,600 synthetic GPR data with 800 sampling steps and 99 traces were generated to pre-train the feature extraction network of the R^2DCNN for classification. In total, it took approximately a month to generate all the 30,574 synthetic GPR data, including 1974 GPR data for training and fine-tuning the R^2DCNN and 28,600 GPR data for pre-training the feature extraction network of the R^2DCNN.

Table 1
Data distribution in dataset.

Dataset	Crack	Void	Separation	Crack_void	Void_ separation	Crack_ separation	Rebar
Water-free defects	132	150	150	133	150	150	150
Water-bearing defects	150	150	150	150	150	150	

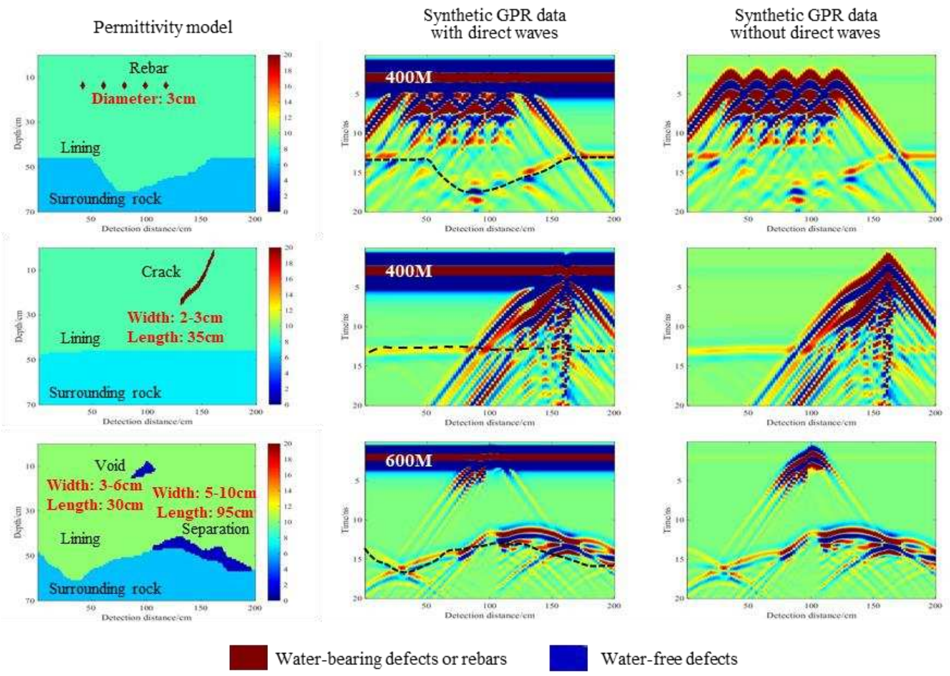

Fig. 2. The permittivity model of tunnel lining internal structure and its corresponding synthetic GPR data before and after removing direct waves. The water-bearing defects or rebars and water-free defects are represented by different colors.

2.2. Real GPR data

To verify the applicability of the proposed method in practical situations, model experiments were performed to obtain real GPR data using a 600 MHz Impulse Radar as the GPR, as shown in Fig. 3. A sandbox was exploited to simulate the tunnel lining internal structure, while acrylic boxes and waterproof boxes were used for simulating cracks and voids within the tunnel lining, respectively. Furthermore, acrylic boxes and waterproof boxes with different rotated angles were deployed at various positions and depths in the model of different depths to increase the diversity of real GPR data. The number of samples per trace and the trace-interval distance of this GPR device were 512 and 0.01 m, respectively.

Fig. 3. The sketch of model experimental environment. (a) Simulated underground structure defects; (b) Acrylic box for the simulating crack; (c) Waterproof box for the simulating void; (d) GPR system utilized in the experiment; (e) Experiment after increasing the height of the model.

Unlike synthetic GPR data, real GPR data is inevitably accompanied by noise signals because of the heterogeneity of the subsurface medium, mutual wave interactions, and the influence of external conditions during data collection. Therefore, these data should be subjected to visualization enhancement using pre-processing techniques, such as time-zero correction, clutter removal, and noise reduction. After a series of pre-processing techniques, the real GPR data with 10 ns of depth in a two-way time domain and 2 m of spacing in the horizontal direction was obtained due to the limitation of sandbox depth. Their morphology patterns varied in terms of abnormal objects and complex geological structures. In total, 118 real GPR data comprising diverse reflected signals representing rebars as well as various structural defects, including voids, cracks, and separations, were obtained.

2.3. GPR image annotation

In this study, additional 28,600 synthetic GPR data with 800 sampling steps and 99 traces, mentioned in Section 2.1, were converted into images with resolutions of 224 × 224 pixels to pre-train the feature extraction network of the R^2DCNN for classification. They need not be annotated by inclined rectangular boxes using the LabelImg software. Therefore, a total of 2092 GPR datasets were used for annotation, including 1974 synthetic GPR datasets and 118 real GPR datasets, to train the R^2DCNN. For subsequent image annotation, 2,092 GPR datasets (800 sampling steps and 99 traces) were converted into images with resolutions of 533 × 533 pixels. The reflected signal features of each GPR image could be related to specific types of tunnel lining internal objects. In particular, the reflected signals generated by the abnormal objects may have phases that are reversed compared with that of the direct waves when the permittivity of the abnormal objects is higher than that of the tunnel lining [11]. Therefore, different objects can be distinguished and discriminated based on the reflected signal features of their GPR images. The object determination of real GPR images primarily depends on the position and type of the object buried in the sand, whereas the abnormal objects of synthetic GPR images were annotated according to the established permittivity model and the GPR image corresponding to the model. Finally, GPR image annotation was manually performed using the open-source software LabelImg in which dissimilar objects were framed using inclined rectangular boxes in various categories in GPR images with resolutions of 533 × 533 pixels. These GPR images were randomly divided into a training set including 1,300 synthetic GPR images and 38 real GPR images, a validation set of 290 synthetic GPR images, and a test set including 384 synthetic GPR images and 80 real GPR images according to the types of images to ensure equal distribution in each type for training and fine-tuning the R^2DCNN.

3. Methodology

Although object detection networks based on horizontal rectangular boxes can detect abnormal objects in GPR images [28-29], they cannot accurately delineate the locations of the distributed reflected signals with arbitrary orientations in GPR images. For example, for crack defects shown in Fig. 1, object detection networks based on horizontal rectangular boxes may produce relatively large regions, which cannot locate the objects very precisely. Thus far, various object detection networks based on inclined rectangular boxes have been used for detecting objects with arbitrary orientations [26,30-31]. However, such networks cannot achieve ideal detection for GPR images of the tunnel lining for several reasons described in Section 1. Therefore, it is essential for deep learning networks to have powerful feature representation and feature fusion abilities to learn various abnormal objects adaptively and generalize the trained models for application to real GPR images with limited data.

In view of the characteristics and challenges related to the GPR images of tunnel linings, we developed an improved R^2DCNN method based on the R^2CNN architecture for automatic detection of abnormal objects with arbitrary orientations in complex GPR images. The R^2DCNN can improve the rapidity and intelligence of detection methods, laying a solid foundation for the automated inspection of tunnels in the future. The R^2DCNN comprises inter-related modules, specifically, DC, feature fusion, and rotated region detection modules. The flowchart of the R^2DCNN is shown in Fig. 4. Firstly, a DC based feature extraction network is employed to extract powerful features from original GPR images with the irregular convolution kernels that change their shape according to the shape of the object. Secondly, the feature fusion module that concatenates the shallow and deep feature maps in the feature extraction network provides a rich feature map with both detailed and semantic information for the following detection. Finally, rotated region detection is used to perform image classification and regression on a series of candidate boxes obtained through region proposal network (RPN) using multi-scale ROI Align, so as to obtain the final detection results. The specific structure of each module is illustrated in Fig. 5. The following sections will describe each of the corresponding modules in detail.

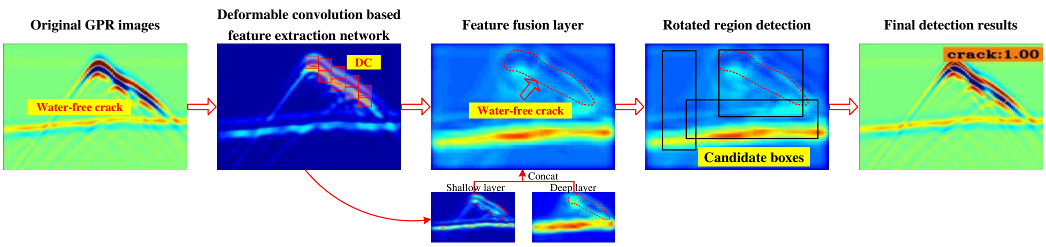

Fig. 4. The flowchart of the R^2DCNN.

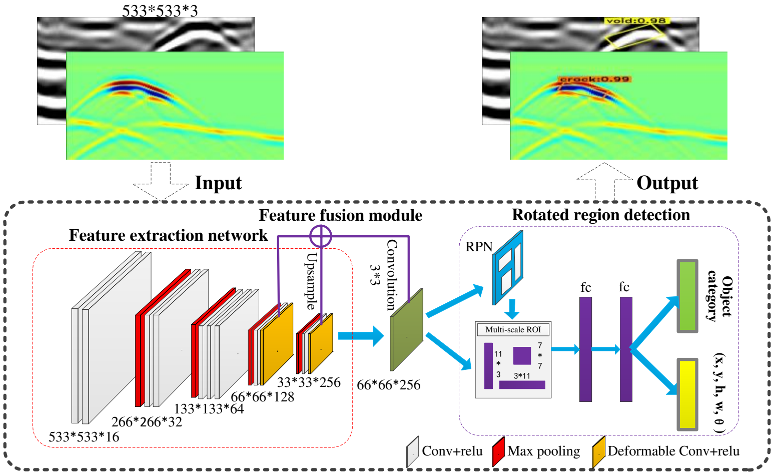

Fig. 5. The network structure of the R^2DCNN.

3.1. Deformable convolution based feature extraction network

The reflected signals of the GPR images show considerable diversity and irregularity due to the various geometric shapes and filling materials of the complex tunnel lining defects. In addition, unpredictable interference in the real world may induce significant noise in the real GPR images, thereby diversifying and complicating the GPR images under the influence of noise. However, real GPR images obtained by model experiments are limited. Thus, it is preferable for deep learning networks to learn the geometric transformations of reflected signal morphologies adaptively and generalize the trained models for application to real GPR images with limited data. CNNs with fixed sampling locations are inherently limited for modelling geometric transformations [32]. DC realizes anisotropic sampling by learning the offsets of the sampling points, as shown in Fig. 6 (a). Therefore, a DC module that can adapt to various reflected signals with different sizes and shapes was introduced into the feature extraction network, as shown in Fig. 5.

The backbone network is based on VGG16 [33], consisting of five convolution blocks (Conv1, Conv2, Conv3, Conv4, and Conv5), a max pooling layer following each convolution block, and the activation function, ReLU, which is used after each convolution layer. The max pooling layers are mostly utilized to reduce the size of the feature map, making it focus on important areas. The activation function is employed to ensure that the values in the feature map are within a reasonable range. Moreover, to reduce the computational burden on the feature extraction network, the number of channels of the feature maps in the five convolution blocks was modified and varied block-wise, as shown in Fig. 5. In this study, DC with learned offsets and a modulation mechanism derived from Deformable ConvNets v2 [22] were employed because of the blurred boundaries between the object and background in the GPR images of the tunnel lining. To better utilize the DC to produce superior detection results, two DCs were added to the relatively backward convolution layers, containing Conv4_2 and Conv5_2 of the feature extraction network, which are more sensitive to the position information of the GPR images [32], and the numbers of convolutional layers in the latter two convolution blocks were reduced accordingly. Meanwhile, atrous convolution with a dilation of 2 was used in the DC module to increase the receptive fields of the offsets and modulation learning with the same complexity as common convolution in terms of the parameters and computation. The offsets of the sampling points, which are learned from the preceding feature maps in the standard convolution, and the modulation mechanism, which adjusts the scope of deformation modelling, enable better adaptation to the sizes and shapes of the reflected signals without the influence of irrelevant content, such as noise, diffraction signals, and multiple waves in the GPR images, thereby preventing the spread of samples beyond the area of interest.

Owing to the different characteristics of the GPR images and natural images, GPR images were chosen (instead of ImageNet) to pre-train the feature extraction network for classification. To achieve pre-training of the feature extraction network, two fully connected layers followed by dropout and the softmax layer were added. The dropout layers following fully connected layers were applied to combat the overfitting problem. The obtained pre-trained model parameters were exploited to initialize the CNN model of the R^2DCNN.

3.2. Feature Fusion Layer

Conventional CNNs, such as R^2CNN, only use the feature learned from the last convolutional layer of the network to perform image classification and regression by multi-scale ROI Align, which provides more semantic information but less details. This method may compromise the accuracy of the location information that is crucial for abnormal object detection in GPR images because the sizes and shapes of the abnormal objects are changeable. In particular, cracks with large aspect ratios can be regarded as small objects [34], the boundaries between the objects and background are blurred in GPR images of tunnel linings, and multiple waves and scattering are produced by water-bearing defects. The features of the lower layer contain more detailed information, such as information regarding the underlying texture and color, but the semantic information is less abundant. Therefore, the feature fusion layer is employed for detection instead of using the last feature map to improve the detection effect for multi-scale objects in complex GPR images.

In terms of the sizes of abnormal objects in GPR images and the receptive field of the feature extraction network, rich multi-scale features of the low-level layer Conv4_2 and high-level layer Conv5_2 are fused, as shown in Fig. 6 (b). The sizes and numbers of feature maps vary for different layers, which implies that the fusion layers are not directly stacked together. Thus, the feature map of the same size as Conv4_2 is generated by upsampling Conv5_2 using nearest neighbor interpolation. Subsequently, the layers of Conv5_2 and Conv4_2 are concatenated along their channel axis to perform fusion. Thereafter, 3 × 3 convolution is utilized to generate the final fusion feature maps for detection to eliminate the aliasing effect of the upsampling and adjust the number of channels of the feature map.

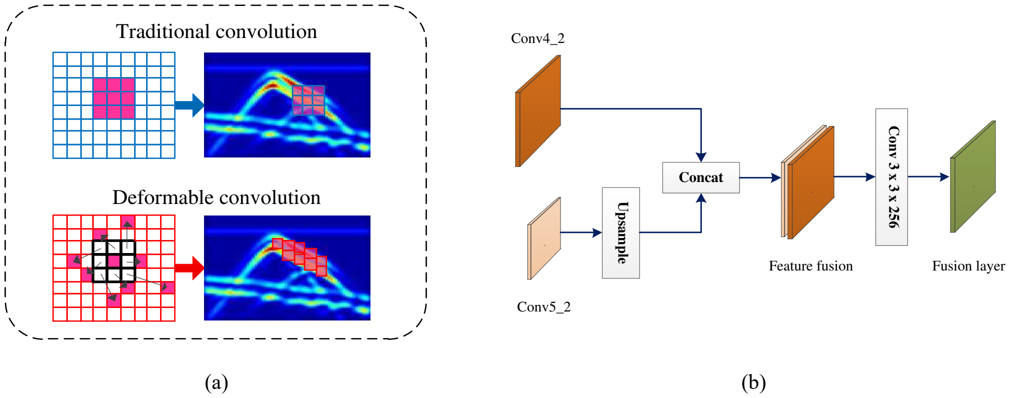

Fig. 6. (a) Different calculation positions under traditional convolution or deformable convolution; (b)Architecture of feature fusion module.

3.3. Rotated region detection

For the detection of tunnel lining abnormal objects using GPR images, horizontal region detection with a relatively large redundant region is not feasible because of the arbitrary orientations of the reflected signals in GPR images. Rotated region detection based on R^2CNN was introduced into the proposed network to enable accurate detection of abnormal objects with arbitrary orientations.

As shown in Fig. 5, the rotated region detection also involves a RPN and Fast R-CNN, which share a common feature extraction network. The RPN is employed to generate a set of horizontal proposals that may enclose the reflected signals of the input GPR images. Thereafter, each horizontal proposal obtains feature maps of different sizes (7 × 7, 11 × 3, 3 × 11) through the multi-scale ROI Align layer to preserve the complete feature information. The Fast R-CNN stage only predicts inclined rectangular boxes (x, y, h, w, and α), which are represented using the coordinates of the center points, the height, width, and rotated angle of the rectangular box [34]. The classification is conducted using concatenated multi-scale features, and the final inclined rectangular boxes are obtained by inclined non-maximum suppression.

4. Experimental results and discussion

This section is divided into four parts. Section 4.1 describes the experimental details and introduces the evaluation indicators. Section 4.2 presents the comprehensive comparative experiments and results on synthetic GPR images. Section 4.3 conducts model verification experiments to discuss the results of the R^2DCNN on real GPR images. Finally, Section 4.4 presents discussion.

4.1. Experimental details and evaluation indicators

The training of the R^2DCNN consists of two main stages. The first stage was used to obtain pre-training model parameters by pre-training the feature extraction network for classification using 28,600 synthetic GPR images. The second stage was utilized to obtain a detection model of defects and rebars within the tunnel lining by training and fine-tuning the R^2DCNN using the pre-trained model parameters and 2092 synthetic and real GPR images with different frequencies described in Section 2. Before training the network, the intensity values of the GPR images were standardized to enhance their contrast.

Our method was implemented on the TensorFlow framework, and an Intel Xeon (R) Gold 5118 CPU with a GTX 1080 Ti GPU was employed for training. In the pre-training phase of the feature extraction network, the input GPR image was resized to 224 × 224. The Adam [35] optimization algorithm was employed during 50 epochs of training. The weight decay and batch size were 0.0005 and 50, respectively. The initial learning rate remained 5e–5 for the first 25 epochs and decayed to 5e–6 at epoch 25. For the R^2DCNN, the GPR image remained the original size of 533 × 533. The training step was 50,000 epochs with an initial learning rate of 5e–5, and the learning rate decay strategy was stepped at the 20,000th and 40,000th epochs with a coefficient of 0.1. The weight decay and batch size were 0.0005 and 1, respectively. The multi-task loss containing cross-entropy loss for classification and smooth L1 loss for regression was utilized to optimize the R^2DCNN through the Adam optimization algorithm.

Although the training of the R^{2}DCNN may take a relatively long time, the detection time for a GPR image would be significantly short.

In our experiment, recall, precision, F-measure, and average precision (AP) were used as evaluation indicators for the detection of internal defects and rebars in the tunnel lining. Recall and precision are the basic indicators to measure the performance of an algorithm under a specific Intersection over Union (IoU) between the predicted boxes and ground truth. The F-measure is the weighted average of recall and precision. The AP, average precision under different recalls, is a comprehensive evaluation indicator that is not affected by the selected thresholds. The mean average precision (MAP) is the average of the AP across all the different defect types.

4.2. Experimental results

This section conducts a comprehensive comparative experiment using synthetic GPR images to confirm the superior performance of the R^{2}DCNN. The ablation experiments were initially performed on synthetic GPR images. Comparisons with the existing optimal methods were subsequently conducted. Finally, we present comparisons of evaluation indicators for various methods.

4.2.1. Ablation experimental results

We benchmarked the R^{2}DCNN along with variant architectures using our synthetic and real GPR images of the tunnel lining to evaluate the contribution of each module in our model, such as the feature fusion and DC modules. Notably, the feature extraction network of the R^{2}DCNN without DC is VGG16.

Fig. 7 presents the results of the R^{2}DCNN along with those of variant methods for synthetic GPR images with different frequencies. The detection result is a GPR image with inclined rectangular boxes used to locate the object, a defect type of each box, and a confidence of each box in the upper right corner that indicates the probability that the object is of this type. In Fig. 7, the first column presents the permittivity model corresponding to the GPR image, the second column presents GPR images with different frequencies, and the third, fourth, and fifth columns provide the detection results of the R^{2}DCNN without DC, R^{2}DCNN without fusion, and R^{2}DCNN, respectively. It can be seen from Fig. 7 that the R^{2}DCNN can accurately locate various reflected signals of GPR images with precise inclined rectangular boxes, whereas there are missing detected objects and imprecise detection boxes in the results of the other variants. These observations indicate that the feature fusion module, which provides accurate location and shape information, together with the DC module, which achieves anisotropic sampling, can jointly improve the ability to detect various abnormal objects with irregular shapes of GPR images with different frequencies in tunnel linings.

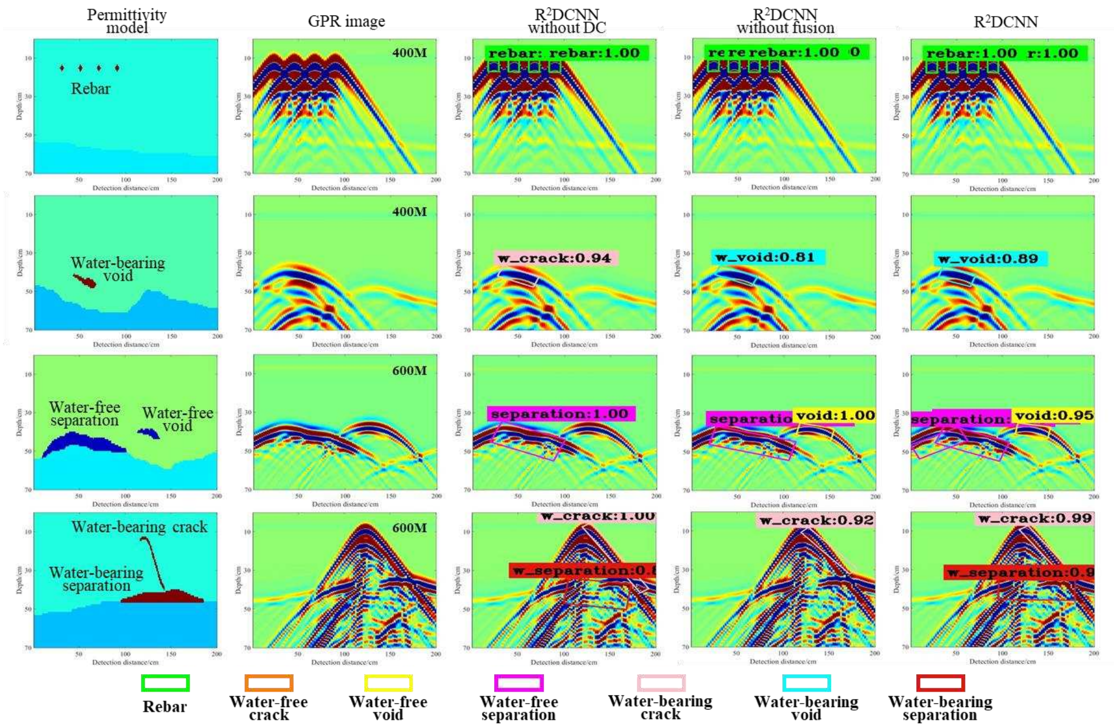

Fig. 7. Object detection results of the R^{2}DCNN along with variant methods when applied to synthetic GPR images with different frequencies. Different types of abnormal objects are indicated by boxes of different colors, as shown in the last row.

4.2.2. Comparative study and results

We selected two well-known methods, the Faster R-CNN for buried object detection using B-scan GPR images [36] and the R^{2}CNN for scene text detection [26], for comparison to verify the effectiveness and superiority of the R^{2}DCNN in tunnel lining defect detection.

Fig. 8 shows the object detection results obtained by applying different methods to synthetic GPR images, including GPR images of single and combined defects as well as synthetic GPR images with defects of different types and conductivities compared to those in the training set. The first column depicts the permittivity model corresponding to the GPR image; the second column shows the GPR images with different frequencies; and the third, fourth, and fifth columns present the detection results of the Faster R-CNN, R^{2}CNN, and R^{2}DCNN, respectively. As shown in Fig. 8, the R^{2}DCNN can accurately locate all abnormal objects in the GPR images, whereas the other two methods produce relatively poor detection results. The Faster R-CNN is designed to generate horizontal rectangular detection boxes including more background with relatively large redundant regions. Moreover, certain detection results cannot be accurately marked or are overlooked. The R^{2}CNN is used for the detection of inclined rectangular boxes, which can address the problem of the detection of abnormal objects with arbitrary orientations in GPR images. But as a result of inaccurate prediction of the direction information of inclined rectangular boxes, this method cannot conduct accurate detection of abnormal objects in GPR images. Additionally, for certain abnormal objects with large changes in shape and unknown forms, the other two methods may yield missing, redundant, or false object detection boxes. These observations indicate that the adaptability and transferability of the two methods are weak. The R^{2}DCNN performs well in a variety of situations and is more adaptive to the detection of various reflected signals with arbitrary orientations of GPR images with different frequencies in tunnel linings.

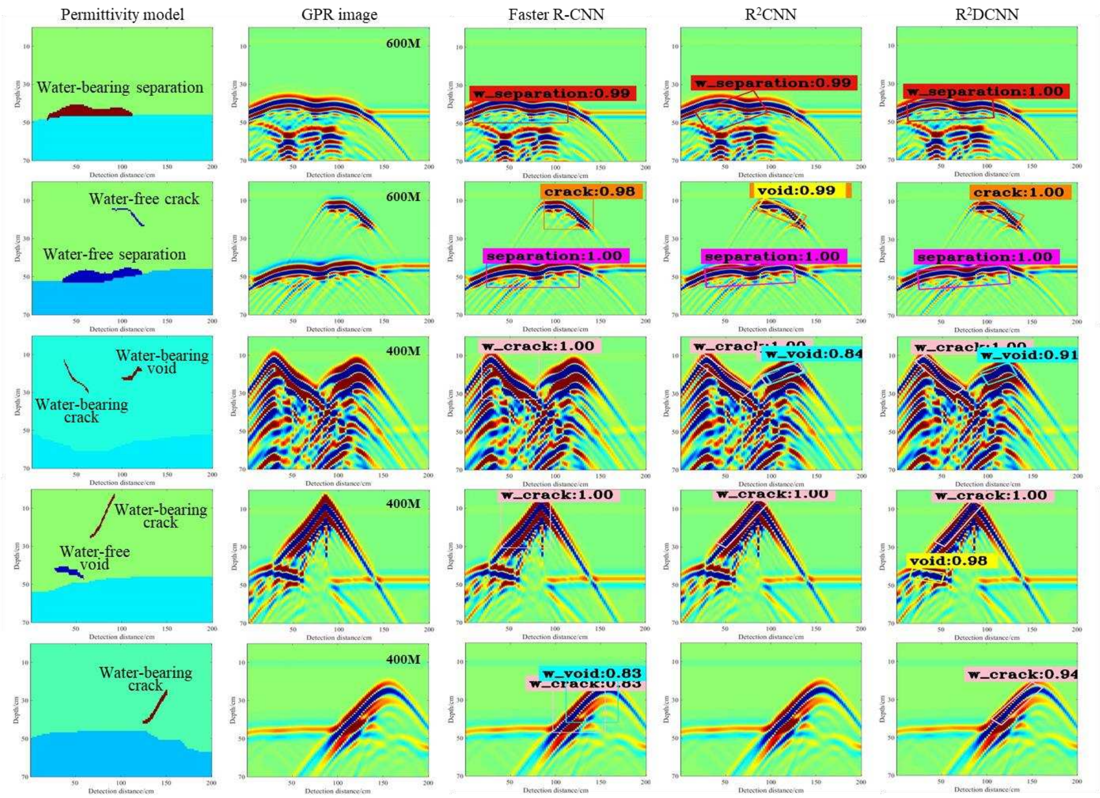

Fig. 8. Object detection results of different methods when applied to synthetic GPR images with different frequencies, containing GPR images of single (the first row) and combined (the middle two rows) defects along with GPR images with defects of different types and conductivities compared to those in the training set (the last two rows).

4.2.3. Comparisons of evaluation indicators

To quantitatively evaluate the performance of various methods and the effect of each module on the model performance, the evaluation indicators detailed in Section 4.1 are utilized to assess the comprehensive performance of the R^{2}DCNN along with other methods when applied to GPR images. Table 2 compares the overall performances of the different methods on synthetic GPR images. The R^{2}DCNN achieves competitive results with a recall of 81.11%, a precision of 87.46%, an F-measure of 84.07%, and a MAP of 73.91% when applied to synthetic GPR images.

For synthetic GPR images, the R^{2}DCNN is slightly worse than the Faster R-CNN, but considerably better than the R^{2}CNN for all indicators. The R^{2}DCNN can locate various abnormal objects more accurately with inclined rectangular boxes, which have the smallest enclosing areas. And few objects were repeatedly detected, as evidenced by the visual outputs. Therefore, for abnormal objects with larger aspect ratios, if the box size and location are not sufficiently precise, the recall and precision decrease easily, making the indicators have lower values than when the Faster R-CNN is applied. According to the results from Table 2, R^2DCNN without fusion achieves 2.97% and 4.21% performance gains in F-measure and MAP, respectively, compared to the R^2CNN. Adding the feature fusion module to the R^2CNN also improves the F-measure by 2.28% and MAP by 3.09%. This confirms that powerful feature representation and feature fusion abilities both contribute towards improved detection in complicated GPR images. The R^2DCNN provides greater improvements compared to other variant methods. The F-measure and MAP are improved by 5.62% and 8.21%, respectively. Meanwhile, our method only consumes a little time (0.0877s) for detecting a GPR image using the configuration described in Section 4.1 (Table 3). And it also increases little time cost compared to the R^2CNN baseline. This means that the R^2DCNN can detect GPR images with higher accuracy and little time cost. Therefore, our proposed method can provide a more accurate suggestion for a less experienced analyst with very little time cost, which can save a considerable amount of time for tunnel lining defect detection. In summary, the R^2DCNN is superior to the other methods when applied to GPR images with different frequencies in tunnel linings.

As can be seen from the object detection results and evaluation indicators of the R^2DCNN along with other methods on GPR images, only using the DC or feature fusion module could not produce good experimental results. The two modules need to be introduced simultaneously to enhance the stability and generalization of the network. The R^2DCNN is more sensitive to abnormal objects in complex GPR images than the other methods, thereby exhibiting appropriate stability and robustness when applied to GPR images with different frequencies in tunnel linings.

Table 2

Comparison of experimentally obtained indicators for synthetic GPR images.

Methods	Recall	Precision	F-measure	MAP
Faster R-CNN	0.8166	0.9113	0.8601	0.7668
R^2CNN	0.7473	0.8285	0.7845	0.6570
R^2DCNN without DC	0.7731	0.8474	0.8073	0.6879
R^2DCNN without fusion	0.7799	0.8553	0.8142	0.6991
R^2DCNN	0.8111	0.8746	0.8407	0.7391

Table 3

Detection time of the R^2DCNN and R^2CNN.

Methods	R^2CNN	R^2DCNN
Time	0.0842s	0.0877s

4.3. Results on real GPR images

Because we aim to apply the R^2DCNN to practical situations, it is vital to demonstrate the applicability and effectiveness of the R^2DCNN using real GPR images. Compared to the synthetic GPR images, real GPR images produce reflected signals with more prominent irregularity and complexity under the influence of considerable noise due to the unpredictable interference in the real world. Moreover, real GPR images are limited. Hence, three real GPR images with rebars and water-free voids of different rotation angles, depths, and positions were used to evaluate our scheme; different depth sandbox models were also used. Fig. 9 compares the results of the R^2DCNN with those of some existing algorithms on real GPR images. The first column depicts the sandbox model corresponding to the GPR image; the second column shows the real GPR images obtained by sandbox model experiments; and the third, fourth, and fifth columns present the detection results of the Faster R-CNN, R^2CNN, and R^2DCNN, respectively. Because the depth of the sandbox models presented in Fig. 9 is different, the position of the interface of the GPR image corresponding to the sandbox model is also inconsistent. Moreover, the signal below the interface of the GPR image is generated by the medium under the sandbox, which is not related to the medium inside the sandbox. For rebars and defects under rebars of the third row in Fig. 9, these three methods fail to recognize the right defect under rebars due to the weaker signal caused by the interference of reflected signals from rebars. Except for defects under rebars, the R^2DCNN can accurately locate abnormal objects with arbitrary orientations on real GPR images, while the Faster R-CNN produces missing and imprecise object detection boxes with relatively large redundant regions, and the R^2CNN produces missing object detection boxes that face difficulty in detecting the real GPR image. In summary, the R^2DCNN obtains convincing detection results, far superior to other methods. The comparative results indicate that the R^2DCNN can be applied to complicated datasets effectively, thereby providing a good basis for the recognition of real GPR images.

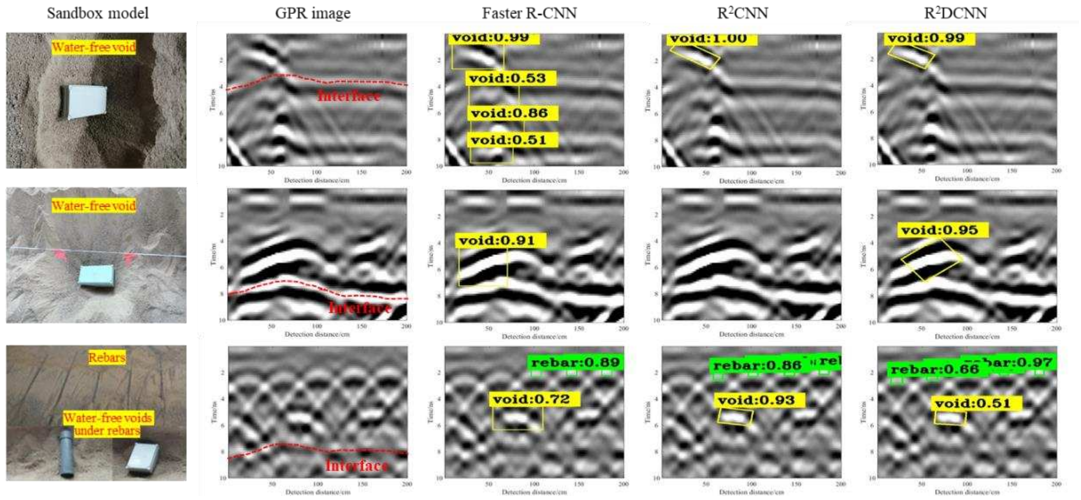

Fig. 9. Object detection results of different methods when applied to real GPR images.

4.4. Discussion

An ablation and comprehensive comparative experiment with the existing optical methods, as well as model verification experiments, are performed as described in Section 4.2 and 4.3. The results confirm that the R^2DCNN overcomes the negative effects of complicated real GPR images with limited data in the tunnel lining and exhibits good stability and generalization when applied to GPR images with different frequencies. For further verification of the feasibility of the R^2DCNN, the intermediate processes of the network are visualized.

The reflected signals of GPR images yielded by abnormal objects of different sizes and shapes within the tunnel lining show diversity and irregularity, and the real GPR images are limited and accompanied by considerable noise. It is difficult to detect abnormal objects of various shapes and sizes on more complex GPR images using traditional convolution because of the fixed sampling location. Hence, a DC module, composed of offset learning of sampling points and a modulation mechanism, was introduced, making the sampling points more suitable for the shapes and sizes of the abnormal objects in GPR images than if a fixed rectangular form had been used.

For improved understanding of the behavior of the DC module, we visualized the spatial support of the network nodes using their effective sampling locations and compared those of DC with traditional convolution methods using synthetic GPR images. The standard operations in DC were neglected because they did not affect the offsets of the sampling points. Fig. 10 shows the relative contributions of these sampling locations to the network nodes. The two different types of GPR images with different frequencies are shown in the first two and last two rows of Fig. 10. The receptive field and sampling locations in the standard convolution were fixed, whereas the DC module adaptively adjusted them according to the sizes and shapes of the abnormal objects. Although GPR images are different from natural images because of the existence of considerable clutter interference and abnormal objects with relatively large aspect ratios in GPR images, the spatial support of DC can approximately cover the entire object and enable better adaptation to various objects when the nodes are on the abnormal objects in GPR images. In the first column of Fig. 10, all sampling points in the DC are more widely distributed when the nodes are in the background of the GPR images. Therefore, DC enables better detection of different types of abnormal objects within the tunnel lining according to the shapes and sizes of the reflected signals from abnormal objects in GPR images.

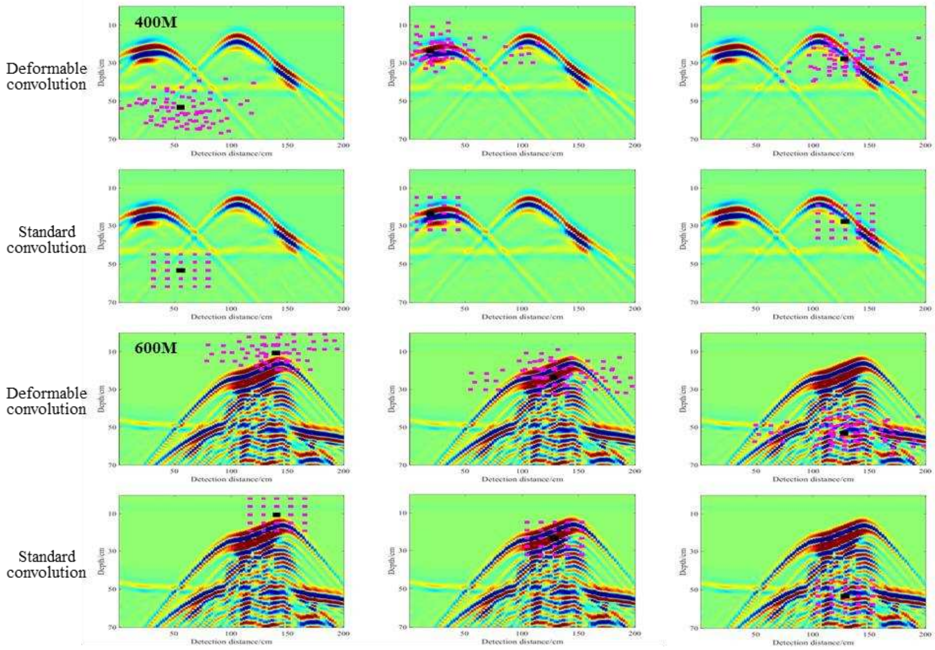

Fig. 10. Spatial support of network nodes in deformable and standard convolution networks. The visualized nodes (center points in black for synthetic GPR images with different frequencies) are in the background (left) and on abnormal objects in the GPR images (middle and right).

The boundaries between the object and background are blurred in the GPR images of the tunnel lining due to diffraction signals, and multiple waves and scattering are induced by water-bearing defects. The feature fusion module was exploited to reuse the feature information. The module combines the advantages of shallow features (Conv4_2) that provide accurate location and shape information and deep features (Conv5_2) that contain more semantic information. The shallow, deep, and fused feature maps were visualized on synthetic and real GPR images, as shown in Fig. 11, to demonstrate the role of the feature fusion module more clearly. The first and second rows present the visualizations of the synthetic and real GPR images, respectively. For the shallow feature maps in the second column, multiple objects in the GPR images represented different specific types of defects. Subsequently, the areas of interest were circled using dashed lines of different colors. In Fig. 11, all defects of shallow features in the second column contain more detailed information than deep features in the third column, such as those related to the underlying texture, shape, and location; the deep features produce large swaths of highlighted information, which is semantic information about the defects, and there is no clear information about the location or shape; the feature maps fusing the shallow and deep features in the fourth column contain the detailed information, wherein the defects that are circled using dashed lines of different colors have dark and bright colors that are extremely similar to the shallow features, and semantic information, wherein the outsides of the defects surrounded by dashed lines of different colors have large swaths of highlighted information that are similar to those of the deep features. This observation further confirms the effectiveness of the feature fusion module when applied to GPR images.

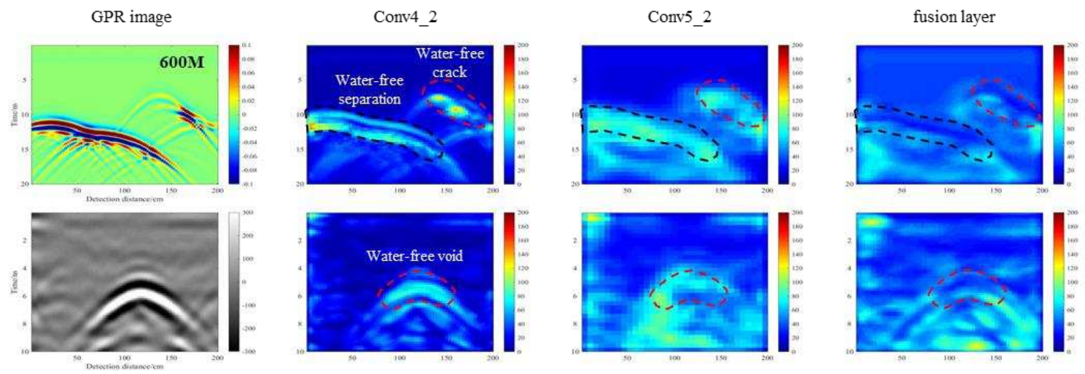

Fig. 11. Visualization of feature fusion module effects using synthetic and real GPR images.

5. On-site experiments

The R^2DCNN produced convincing results upon application in real GPR images obtained by model experiments, which reflects its excellent adaptability, and it can be used in engineering due to the greater similarity between real GPR images collected from the model experiments and practical tunnels. To further verify the applicability of the proposed method in engineering, it was implemented to automatically detect reflected signals in GPR images obtained from the surveys of multiple tunnels, such as the Nanshibi Tunnel in Jiangxi Province and the Shuiquanwan Tunnel in Shanxi Province. The implementation process of the proposed method in practical tunnels is summarized in Fig. 12.

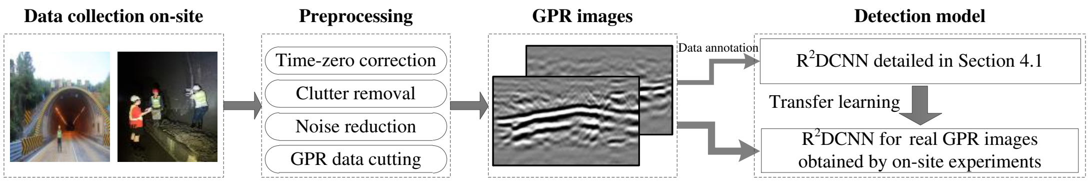

Fig. 12. The implementation process of the proposed method in practical tunnels.

Firstly, it is necessary to collect a large amount of raw GPR data at the tunnel site through GPR equipment to verify the proposed method. During this verification process, a 600 MHz Impulse Radar system was used to scan multiple tunnel walls to collect the GPR data on-site. The number of samples per trace and the trace-interval distance of this GPR device were 512 and 0.01 m, respectively. Secondly, certain pre-processing techniques were employed to highlight the reflected signals from tunnel lining defects and obtain the GPR data of the corresponding size. A total of 219 GPR data were obtained, in which each GPR data covered a detection distance of 2m and a time window of 20ns in depth over the tunnel lining. The GPR data was then converted into images with resolutions of 533 × 533 pixels to fine-tune and test the R^2DCNN. Unlike synthetic GPR data, real GPR data is inevitably accompanied by considerable noise. Therefore, it is difficult for the R^2DCNN, trained through both synthetic and real GPR images obtained from the previously described sandbox experiments, to directly test the GPR images collected from practical tunnels. Thus, after a series of pre-processing techniques, only 99 GPR images were annotated to fine-tune the R^2DCNN (based on R^2DCNN weights in Section 4.1), and the number of iterations was 10000. The training time of the R^2DCNN was approximately 3 hours. Finally, the detection model of defects and rebars was utilized to detect abnormal objects of the specific tunnel.

Fig. 13 depicts the results of the R^2DCNN on the remaining 120 GPR images. The first row shows the real GPR image collected from practical tunnels, and the second row shows the detection results of the R^2DCNN. It can be seen that the R^2DCNN produces superior detection results. In particular, the R^2DCNN could detect small abnormal objects in GPR images in the first column of Fig. 13. The practical tunnel we selected for on-site experiments has a large number of structural defects, which needed to be repaired by reinforcing the surrounding rock after the lining. Therefore, grouting pipes were hit in the tunnel to reinforce the surrounding rock. Considering that the defect inside the tunnel lining is concealed, the GPR images collected from a tunnel lining with grouting pipes are utilized to further demonstrate the adaptability of our proposed method. The detection results are shown in Fig. 14. The R^2DCNN can accurately locate and recognize reflected signals from grouting pipes in the GPR image. The reflected signals are recognized as a water-bearing void because of the similar defect characteristics between the grouting pipe and the water-bearing void. The evaluation indicators detailed in Section 4.1 are utilized to analyze the comprehensive performance of the R^2DCNN on practical tunnels, as presented in Table 4. The R^2DCNN produces favorable performance with a recall of 60.13%, a precision of 72.45%, an F-measure of 60.43%, and a MAP of 47.45% when applied to real GPR images collected from practical tunnels. The indicators of real GPR images are slightly lower than those of synthetic GPR images. This gap may be because the real GPR images are limited and more complicated under the influence of noise, revealing various reflected signal morphologies. Thus, the R^2DCNN enables the accurate detection of defects inside the tunnel lining, which proves it is applicable in engineering.

In case of other tunnels, the raw GPR data collected using the GPR equipment needs to be pre-processed (such as time-zero correction, clutter removal, or noise reduction, etc.) to obtain a large number of GPR images with appropriate sizes and clear reflected signals. Subsequently, only a small number of GPR images with reflected signals, manually annotated by inclined rectangular boxes using the LabelImg software, are exploited to fine-tune the R^2DCNN due to the different characteristics of the GPR data collected from different tunnels. As long as the GPR image between the training and test set has similar settings, there is no specific setting for data collection and the size of GPR images. Although it might take a relatively long time for data annotation and network training to obtain a defect detection model for tunnel linings (approximately 4 hours), the detection time for a GPR image would be significantly short (approximately 0.0877 s). Moreover, the model can detect different defect types and their locations. For example, detecting a continuous scan of a tunnel wall, including approximately 10,000 GPR images, might take nearly 16 min using our proposed method, which has a high detection efficiency. As an automatic detection system, it has the potential to analyze more GPR images than a trained analyst in a shorter period, and it can also serve as an aid to a less experienced analyst by suggesting interpretations that might not be obvious.

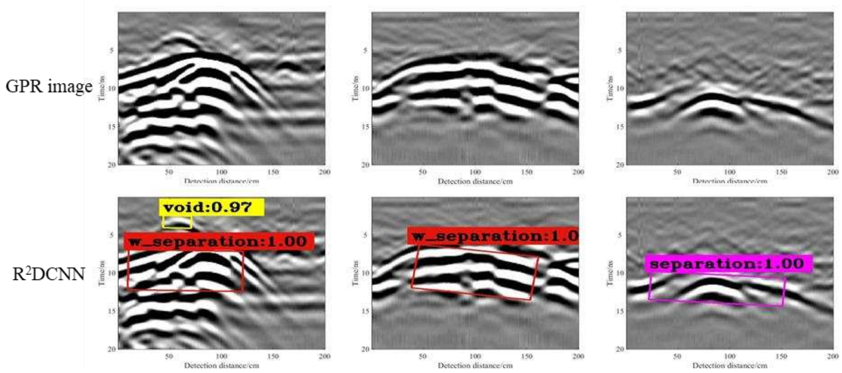

Fig. 13. Object detection results of the R²DCNN when applied to real GPR images collected from practical tunnels.

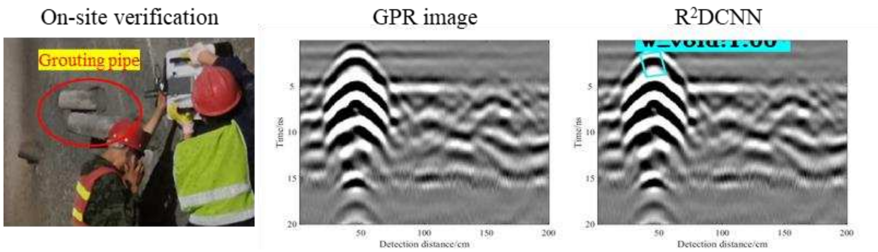

Fig. 14. On-site experiment results.

Table 4

Results of the R²DCNN on real GPR images collected from practical tunnels.

Method	Recall	Precision	F-measure	MAP
R²DCNN	0.6013	0.7245	0.6043	0.4745

6. Conclusions

In this study, we propose the R²DCNN for the automatic detection of abnormal objects with arbitrary orientations in GPR images of tunnel lining, and the following conclusions are obtained.

(1) The R²DCNN is capable of fine-grained feature extraction and has a powerful modelling ability for abnormal objects of various shapes and sizes, using DC, feature fusion, and rotated region detection modules. This method enables accurate detection of defects and rebars of various shapes and sizes with arbitrary orientations in tunnel linings.

(2) A comprehensive comparative study shows that the F-measure and MAP of the R²DCNN are improved by 5.62% and 8.21%, respectively, compared to the R²CNN when applied to synthetic GPR images. And the R²DCNN only increases little time cost for detecting a GPR image compared to the R²CNN baseline. Additionally, a model verification experiment confirms the effectiveness of the R²DCNN on real GPR images. The R²DCNN exhibits appropriate stability and generalization when applied to synthetic and real GPR images with different frequencies, as well as GPR images with defects of different types and conductivities compared to those of the training set in tunnel linings.

(3) On-site experiments are employed to describe the implementation process of the R²DCNN in detail and confirm its effectiveness in practical tunnels. The R²DCNN produces favorable performance with a recall of 60.13% and a precision of 72.45% when applied to real GPR images collected from practical tunnels. As an automatic detection system, it has the potential to analyze numerous more GPR images than a trained analyst in a shorter period. Furthermore, the R²DCNN could serve as an aid to a less experienced analyst by suggesting interpretations that might not be obvious. Therefore, the proposed method can improve the key technical links of automated tunnel inspections in the future and has practical prospects.

(4) Although the R²DCNN achieves suitable results when applied to both synthetic and real GPR images, it poses certain limitations on the diversity of real GPR images. Further experimentation on a larger and more diverse set of real GPR images is required in order to better verify the system performance for practical applications. In our future research, we also wish to compare and analyze the experimental results of the deep learning model using GPR images of different frequencies and sites to verify the stability and superiority of the network.

Acknowledgements

This work was supported by the Joint Program of the National Natural Science Foundation of China [grant number U1806226]; the National Natural Science Foundation of China [grant number 41877230]; the National Key Research and Development Program of China [grant number 2018YFC0406904]; and the Transportation Research Project of Department of

Transport of Shaanxi Province in 2019 [grant number 19-06K]. The third author was partially supported by the Alan Turing Institute.

References

[1] K. Loupos, A.D. Doulamis, C. Stentoumis, E. Protopapadakis, K. Makantasis, N.D. Doulamis, et al. Autonomous robotic system for tunnel structural inspection and assessment, International Journal of Intelligent Robotics and Applications. 2 (1) (2018) pp. 43–66, https://doi.org/10.1007/s41315-017-0031-9.

[2] Y. Jiang, X. Zhang, T. Taniguchi, Quantitative condition inspection and assessment of tunnel lining, Automation in Construction. 102 (2019) pp. 258-269, https://doi.org/10.1016/j.autcon.2019.03.001.

[3] R. Montero, J.G. Victores, S. Martínez, A. Jardón, C. Balaguer, Past, present and future of robotic tunnel inspection, Automation in Construction. 59 (2015) pp. 99-112, https://doi.org/10.1016/j.autcon.2015.02.003.

[4] Z. Tong, J. Gao, H. Zhang, Innovative method for recognizing subgrade defects based on a convolutional neural network, Construction and Building Materials. 169 (2018) pp. 69-82, https://doi.org/10.1016/j.conbuildmat.2018.02.081.

[5] E. Menendez, J.G. Victores, R. Montero, S. Martínez, C. Balaguer, Tunnel structural inspection and assessment using an autonomous robotic system, Automation in Construction. 87 (2018) pp. 117-126, https://doi.org/10.1016/j.autcon.2017.12.001.

[6] V. Krause, I. Abdel-Qader, O. Abudayyeh, S. Yehia, An image segmentation algorithm for the detection of rebar in bridge decks from GPR scans, 2007 IEEE International Conference on Electro/Information Technology, Chicago, IL, USA, 2007, pp. 114-119, https://doi.org/10.1109/EIT.2007.4374476.

[7] W. Lei, M. Man, R. Shi, G. Liu, Q. Gu, Target detection based on automatic threshold edge detection and template matching algorithm in GPR, 2018 IEEE 3rd Advanced Information Technology, Electronic and Automation Control Conference (IAEAC), Chongqing, China, 2018, pp. 1406-1410, https://doi.org/10.1109/IAEAC.2018.8577508.

[8] J. Ma, W. Xu, Thickness Evaluation and Rebar Recognition of Railway Tunnel Lining Based on GPR, Proceedings of the 2015 International Conference on Electrical and Information Technologies for Rail Transportation, Zhuzhou, China, 2015, pp. 665-675, https://doi.org/10.1007/978-3-662-49370-0_69.

[9] Y. Lyu, H. Wang, J. Gong, GPR Detection of Tunnel Lining Cavities and Reverse-time Migration Imaging. Applied Geophysics. 17 (1) (2020) pp. 1-7, https://doi.org/10.1007/s11770-019-0831-9.

[10] N.P. Singh, M.J. Nene, Buried object detection and analysis of GPR images: Using neural network and curve fitting, 2013 Annual International Conference on Emerging Research Areas and 2013 International Conference on Microelectronics, Communications and Renewable Energy, Amal Jyothi Coll Engn, Kanjirapally, India, 2013, pp. 1-6, https://doi.org/10.1109/AICERA-ICMiCR.2013.6576024.

[11] E. Pasolli, F. Melgani, M. Donelli, Automatic Analysis of GPR Images: A Pattern-Recognition Approach, IEEE Transactions on Geoscience and Remote Sensing. 47 (7) (2009) pp. 2206-2217, https://doi.org/10.1109/TGRS.2009.2012701.

[12] Q. Dou, L. Wei, D.R. Magee, A.G. Cohn, Real-Time Hyperbola Recognition and Fitting in GPR Data, IEEE Transactions on Geoscience and Remote Sensing. 55 (1) (2017) pp. 51-62, https://doi.org/10.1109/TGRS.2016.2592679.

[13] X. Zhou, H. Chen, J. Li, An Automatic GPR B-Scan Image Interpreting Model, IEEE Transactions on Geoscience and Remote Sensing. 56 (6) (2018) pp. 3398-3412, https://doi.org/10.1109/TGRS.2018.2799586.

[14] X. Xu, Y. Lei, F. Yang, Railway Subgrade Defect Automatic Recognition Method Based on Improved Faster R-CNN, Scientific Programming. 2018 (2018) pp. 4832972, https://doi.org/10.1155/2018/4832972.

[15] Z. Tong, D. Yuan, J. Gao, Y. Wei, H. Dou, Pavement-distress detection using ground-penetrating radar and network in networks, Construction and Building Materials. 233 (2020) pp. 117352, https://doi.org/10.1016/j.conbuildmat.2019.117352.

[16] Z. Xiang, A. Rashidi, G. Ou, An Improved Convolutional Neural Network System for Automatically Detecting Rebar in GPR Data, ASCE International Conference on Computing in Civil Engineering, Georgia Inst Technol, Atlanta, Georgia, 2019, pp. 422-429, https://doi.org/10.1061/9780784482438.054.

[17] K. Dinh, N. Gucunski, T.H. Duong, An algorithm for automatic localization and detection of rebars from GPR data of concrete bridge decks, Automation in Construction. 89 (2018) pp. 292-298, https://doi.org/10.1016/j.autcon.2018.02.017.

[18] J.K. Alvarez, S. Kodagoda, Application of deep learning image-to-image transformation networks to GPR radargrams for sub-surface imaging in infrastructure monitoring, 2018 13th IEEE Conference on Industrial Electronics and Applications (ICIEA), Wuhan, China, 2018, pp. 611-616, https://doi.org/10.1109/ICIEA.2018.8397788.

[19] H.-Y. Ko, N. Kim, [Performance Analysis of Detecting buried pipelines in GPR images using Faster R-CNN], Journal of Convergence for Information Technology. 9 (5) (2019) pp. 21–26, https://doi.org/10.22156/CS4SMB.2019.9.5.021.

[20] S. Yang, Z.Wang, J.Wang, A.G. Cohn, J. Zhang, P. Jiang et al. Defect segmentation: Mapping tunnel lining internal defects with ground penetrating radar data using a convolutional neural network, arXiv:2003.13120v1 [Preprint]. 2020. Available from: https://arxiv.org/abs/2003.13120.

[21] F. Xu, H. Li, H. Yao, M. An, Tunnel Lining Voids Detection Method Incorporating Guide Anchor Mechanism, International Symposium on Artificial Intelligence and Robotics 2020, Kitakyushu, Japan, 2020, pp. 115740W, https://doi.org/10.1117/12.2579785.

[22] X. Zhu, H. Hu, S. Lin, J. Dai, Deformable ConvNets V2: More Deformable, Better Results, 2019 IEEE/CVF Conference on Computer Vision and Pattern Recognition (CVPR), Long Beach, CA, USA, 2019, pp. 9300-9308, https://doi.org/10.1109/CVPR.2019.00953.

[23] J. Dai, H. Qi, Y. Xiong, Y. Li, G. Zhang, H. Hu, et al. Deformable Convolutional Networks, 2017 IEEE International Conference on Computer Vision (ICCV), Venice, Italy, 2017, pp. 764-773, https://doi.org/10.1109/ICCV.2017.89.

[24] L. Zhang, Y. Zhang, Z. Zhang, J. Shen, H. Wang, Real-Time Water Surface Object Detection Based on Improved Faster R-CNN, Sensors. 19 (16) (2019) pp. 3523, https://doi.org/10.3390/s19163523.

[25] T. Kong, A. Yao, Y. Chen, F. Sun, HyperNet: Towards Accurate Region Proposal Generation and Joint Object Detection, 2016 IEEE Conference on Computer Vision and Pattern Recognition (CVPR), Seattle, WA, USA, 2016, pp. 845-853, https://doi.org/10.1109/CVPR.2016.98.

[26] Y. Jiang, X. Zhu, X. Wang, S. Yang, W. Li, H. Wang, et al. R2CNN: Rotational Region CNN for Orientation Robust Scene Text Detection, arXiv:1706.09579v2 [Preprint]. 2017. Available from: https://arxiv.org/abs/1706.09579.

[27] J. L. Davis, A. P. ANNAN, Ground-penetrating radar for high-resolution mapping of soil and rock stratigraphy, Geophysical Prospecting. 37 (5) (1989)

pp. 531–551, https://doi.org/10.1111/j.1365-2478.1989.tb02221.x.

[28] S. Ren, K. He, R. Girshick, J. Sun, Faster R-CNN: Towards Real-Time Object Detection with Region Proposal Networks, IEEE Transactions on Pattern Analysis & Machine Intelligence. 39 (6) (2017) pp. 1137-1149, https://doi.org/10.1109/TPAMI.2016.2577031.

[29] Z. Zong, C. Chen, X. Mi, W. Sun, Y. Song, J. Li, et al. A Deep Learning Approach for Urban Underground Objects Detection from Vehicle-Borne Ground Penetrating Radar Data in Real-time, ISPRS - International Archives of the Photogrammetry, Remote Sensing and Spatial Information Sciences, Munich, Germany, 2019, pp. 293-299, https://doi.org/10.5194/isprs-archives-XLII-2-W16-293-2019.

[30] L. Zhou, H. Wei, H. Li, W. Zhao, Y. Zhang, Y. Zhang, Arbitrary-Oriented Object Detection in Remote Sensing Images Based on Polar Coordinates. IEEE Access. 8 (2020) pp. 223373-223384, https://doi.org/10.1109/ACCESS.2020.3041025.

[31] Y. Xu, M. Fu, Q. Wang, Y. Wang, K. Chen, G. Xia, et al. Gliding vertex on the horizontal bounding box for multi-oriented object detection. IEEE Transactions on Pattern Analysis and Machine Intelligence. 43 (4) (2021) pp.1452-1459, https://doi.org/10.1109/TPAMI.2020.2974745.

[32] D. Cao, Z. Chen, L. Gao, An improved object detection algorithm based on multi-scaled and deformable convolutional neural networks. Human-centric Computing and Information Sciences. 10 (1) (2020) pp. 14, https://doi.org/10.1186/s13673-020-00219-9.

[33] K. Simonyan, A. Zisserman, Very Deep Convolutional Networks for Large-Scale Image Recognition, arXiv:1409.1556 [Preprint]. 2014. Available from: https://arxiv.org/abs/1409.1556.

[34] X. Yang, H. Sun, K. Fu, J. Yang, X. Sun, M. Yan, et al. Automatic Ship Detection in Remote Sensing Images from Google Earth of Complex Scenes Based on Multiscale Rotation Dense Feature Pyramid Networks, Remote Sensing. 10 (1) (2018) pp. 132, https://doi.org/10.3390/rs10010132.

[35] D.P. Kingma, L.J. Ba, Adam: A Method for Stochastic Optimization, arXiv:1412.6980 [Preprint]. 2014. Available from: http://arxiv.org/abs/1412.6980v8.

[36] M. Pham, S. Lefèvre, Buried Object Detection from B-Scan Ground Penetrating Radar Data Using Faster-RCNN, IGARSS 2018 - 2018 IEEE International Geoscience and Remote Sensing Symposium, Valencia, Spain, 2018, pp. 6804-6807, https://doi.org/10.1109/IGARSS.2018.8517683.